Impact of ice multiplication on the cloud electrification of a cold-season thunderstorm: a numerical case study

Jing Yang[1,2], Shiye Huang[1], Qilin Zhang[1], Xiaoqin Jing[1], Yuting Deng[1], Yubao Liu[1]

[1]Collaborative Innovation Center on Forecast and Evaluation of Meteorological Disasters (CIC-FEMD)/China Meteorological
5 Administration Aerosol-Cloud and Precipitation Key Laboratory/Precision Regional Earth Modeling and Information Center
(PRMIC), Nanjing University of Information Science & Technology, Nanjing, 210044, China.
[2]CMA Cloud-Precipitation Physics and Weather Modification Key Laboratory (CPML), Beijing, 100081, China.

Correspondence to: Yubao Liu (ybliu@nuist.edu.cn)

Abstract. Ice microphysics controls cloud electrification in thunderstorms, and the various secondary ice production (SIP)
10 processes are vital in generating high ice concentration. However, the role of SIP in cold-season thunderstorms is not well
understood. In this study, the impacts of SIP on the electrification in a thunderstorm occurred in late November is investigated
using model simulations. The parameterizations of three SIP processes are implemented in the model, including the rime-
splintering, ice-ice collisional breakup, and shattering of freezing drops. In addition, a noninductive and an inductive charging
parametrization, as well as a bulk discharging model are coupled with the spectral bin microphysics scheme. The results show
15 the simulated storm intensity and temporal variation of flash rate are improved after SIP parametrizations are implemented in
the model. Among the three SIP processes, the rime-splintering and shattering of freezing drops have stronger impacts on the
storm than the ice-ice collisional breakup. The graupel and snow concentration are enhanced while their sizes are suppressed
due to the SIP. The changes in the ice microphysics result in substantial changes in the charge structure. The total charge
density changes from an inverted tripole structure to a dipole structure (tripole structure at some locations) after SIP is
20 considered in the model, mainly due to the enhanced collision between graupel and ice, and riming at temperatures warmer
than -20 °C. These changes lead to an enhancement of vertical electric field, especially in the mature stage, which explains the
improved modelling of flash rate. The results highlight that the cold-season cloud electrification is very sensitive to the SIP.

1 Introduction

Cold-season thunderstorms may have different characteristics of charge structure and lightning activity from warm-season
25 thunderstorms due to the different thermodynamic conditions (Michimoto, 1991; Takahashi et al., 1999; Caicedo et al., 2018).
Caicedo et al. (2018) investigated the differences between cold-season and warm-season thunderstorms in north-central Florida
using the Lightning Mapping Array (LMA) and radar data. They showed an apparent discrepancy is that all the observed
charge areas of summer storms were located up to 1 km higher than in winter/spring storms, as well as the 0 °C, -10 °C, and -
20 °C isotherms. The average LMA initiation power in winter/spring storms was about an order larger than in summer storms.
30 This result is supported by the electric field measurements of the initial breakdown process by Brook (1992), who assured that

cloud-to-ground discharges and intracloud discharges were probably more energetic in winter than in summer. Wang et al. (2021) reported that in contrast to lightning in summer, which mostly delivered negative charges to ground, 30% cloud-to-ground lightning in Honshu Island winter thunderstorms delivered positive charges to ground. They attributed this phenomenon to inverted charge structures. The apparent differences between the cold-season and warm-season thunderstorms indicate

35   different characteristics of ice microphysics that control the cloud electrification.

Extensive studies have been made to understand the role of ice microphysics on cloud electrification in summertime thunderstorms (e.g., Mansell et al., 2010; Fierro et al., 2013; Guo et al., 2005; Qie et al., 2015; 2019; Zhang et al., 2016; Lyu et al., 2023), while fewer have been performed focusing on cold-season thunderclouds. Michimoto (1991) investigated the

40   behaviour of both 30 dBZ and 20 dBZ radar echoes in early winter thunderstorms and found that lighting occurred as 30 dBZ radar echo reached -20 °C, from which it could be inferred that lightning was related to the interaction of graupel and ice crystals. Zheng et al. (2018) analyzed the charge distribution of cells in three winter thunderstorms in Hokuriku region of Japan based on LMA and radar data. They suggested the riming electrification between graupel and ice crystals or their aggregations are the dominant mechanism for the electrification in most cells, and the charging process between snow aggregates is

45   responsible for some inverted charge structure that occurred above 0 °C isotherm. Using a variety of observational data from Video Sounder, Video Sounder-HYVIS, radar, and the Lightning Location System Network, Takahashi et al. (2019) revealed that the frequent lightning activity produced by shallow winter thunderclouds in Hokuriku is probably due to the high number concentration of ice crystals.

50   One of the key mechanisms of ice generation in deep convective cloud is ice multiplication, i.e., secondary ice production (SIP), which means the ice fragments produced during the interactions between different hydrometeors or freezing of supercooled drops. SIP is the main explanation that the observed ice concentration orders of magnitude higher than the ice nucleating particles (INP, Hallett and Mossop, 1974; Heymsfield and Willis, 2014; Yang et al., 2016; Korolev and Leisner, 2020). Some studies have tried to investigate the impact of SIP on cloud electrification in summer (e.g., Fierro et al., 2013;

55   Latham et al. 2004; Mansell et al., 2010; Phllips et al., 2020; Phillips and Patade, 2022), mostly based on numerical simulation since a limitation of observation is it can hardly separate different ice generation processes. For example, Latham et al. (2004) investigated the role of the rime-splintering process in lightning activity using model simulation, they suggested that the relationship between flash rate and precipitation intensity is linear if not considering SIP, while this relationship changed to non-linear with the SIP included. However, the rime-splintering is not the only SIP process that can influence the charge

60   structure of thunderstorm. Secondary ice can be produced through various processes, such as the shattering of freezing drops and ice-ice collisional breakup (Lauber et al., 2018; Phillips et al. 2018; Korolev and Leisner, 2020). Recently, Phillips and Patade (2022) showed the ice-ice collisional breakup may significantly alter the charge structure of summertime thunderstorms based on model simulation.

65 Till now, to our best knowledge, no study has investigated the role of different SIP processes in cloud electrification under
cold-season condition using numerical simulations. But there are a few modelling studies highlighted the importance of ice
generation in wintertime cloud electrification. For example, Takahashi (1983) studied electrical development in winter
thunderclouds using an axisymmetric cloud model. The results showed no strong electrification was observed prior to the
appearance of the solids, which implies the importance of the riming-charging for the electrification. Thus, the generation of
70 graupel perhaps plays a vital role in the wintertime cloud electrification, while SIP controls the fast graupel generation in
convective clouds (Yang et al., 2016; Takahashi et al., 2019). Using Regional Atmospheric Modelling System (RAMS)
mesoscale forecast model, Altaratz et al. (2005) analyzed the charge separation in winter convections using different
parameterizations of noninductive charging mechanism, and they showed the charge structure is very sensitive to the choice
of ice microphysics scheme.

75

In this study, we performed a real-case simulation using Weather Research and Forecast (WRF) model coupled with a fast
spectral bin microphysics (SBM) (Khain et al., 2004) and a bulk lightning model (Fierro et al., 2013) to investigate the impacts
of SIP on cold-season thunderstorm. Parameterizations of three different SIP processes, an inductive and a noninductive
charging parameterization (Saunders and Peck, 1998; Mansell et al., 2005; Mansell, 2010) are implemented in the fast-SBM
80 scheme. The SIP processes considered here include rime-splintering, ice-ice collisional breakup, and shattering of freezing
drops. The rest of the paper is organized as follows: Section 2 describes the model and design of numerical experiments.
Section 3 shows the results, including the model validation and the impacts of different SIP processes on cloud microphysics
and charge structure. Discussion and conclusions are presented in Section 4.

2 Model description and design of numerical experiments

85 **2.1 Case description**

On Nov. 27th-28th, 2022, a severe thunderstorm occurred in Southeast China. The storm began at about 15:00 UTC on Nov.
27th, and lasted for more than 18 hours. Figure 1 shows the synoptic conditions at 18:00, Nov. 27th and 00:00, Nov. 28th plotted
using NCEP reanalysis data. At 500 hPa, the relative humidity was low in southeast China at 18:00, Nov. 27th (Fig. 1a).
Westerly wind prevailed and the temperature ranged from -6 °C to -12 °C. A weak short wave was present between 108 °E
90 and 112 °E, and was moving towards the east. At 850 hPa (Fig. 1b), the southwesterly wind brought warm moist air to southeast
China, the low-level relative humidity was very high, resulting in a nearly saturated condition. Baroclinicity was clearly present
as seen from the wind blowing across the isotherms. The moist low-level and dry high-level condition is favorable for
convection formation. At 00:00, Nov. 28th, two areas with relatively high relative humidity were observed at 500 hPa,
especially near Fuyang, where the air was saturated. This is because two convective cells already formed at this time. The low-
95 level southwesterly wind kept providing warm most air during the development of the convection.
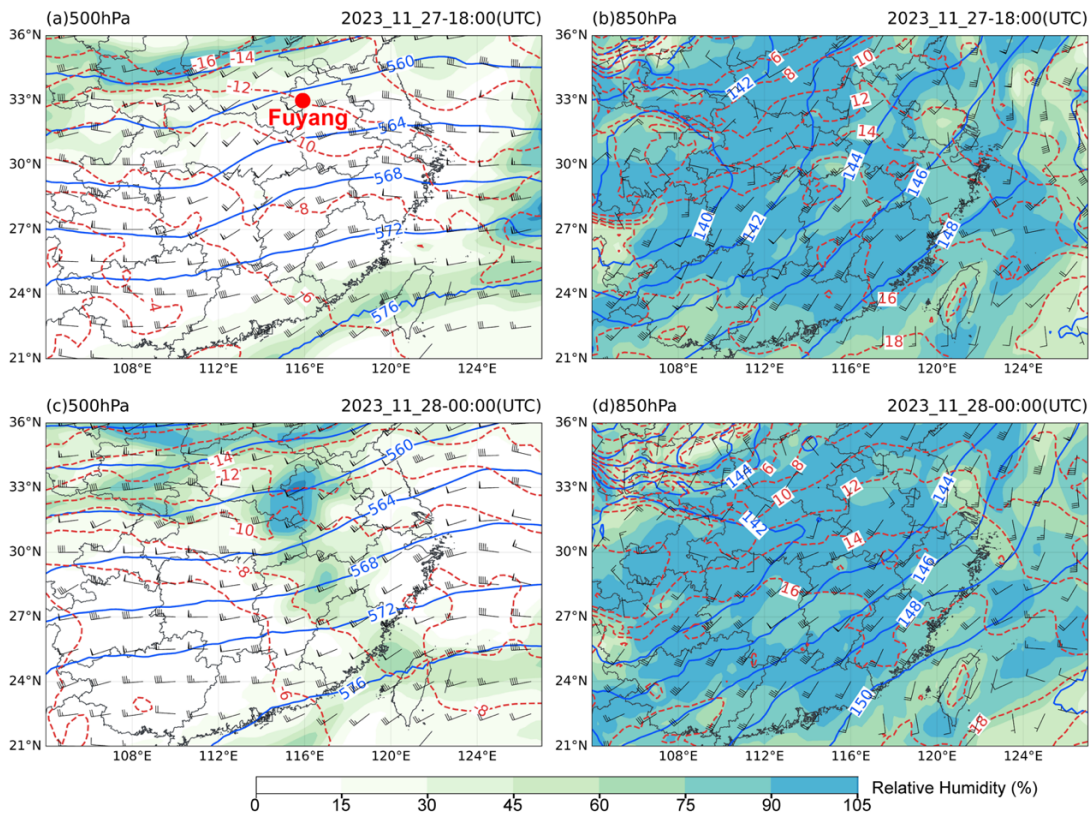
Figure 1: Synoptic conditions of the thunderstorm occurred on Nov. 28ᵗʰ, 2022. (a and b) 500 mb geopotential height, isotherms and wind barbs at 04:00 UTC and 10:00 UTC, respectively. (c and d) Same as (a) and (b) but for 850 mb. The red dot in (a) indicates the location of the sounding measurement that shown in Fig. 2.

100

The synoptic condition is also evident in the sounding measurement. As seen in Figure 2, at 12:00 on Nov. 27ᵗʰ, there was a deep moist layer from surface up to 700 hPa, and the specific humidity decreased substantially above 700 hPa. The low-level wind was southwesterly and the upper-level wind was westerly. Due to the southwesterly warm air, the temperature near surfaces was approximately 18 °C, which is higher than the typical temperature in November in this region, but is about 10 °C

105 lower than that in summer. Potential instability was clearly present in such a thermodynamic environment, providing favorable conditions for deep convection to occur. At 00:00 on Nov. 28ᵗʰ, the air was nearly saturated below 500 hPa, as the convective clouds had formed. There was an inversion layer near surface, probably due to the cold pool induced by the convective precipitation.

110 The radar composite reflectivity at different times in southeast China is shown in Figure 3. At 02:00, Nov. 28ᵗʰ, two deep convective clouds were observed, extending from southwest to northeast and generating lightning flashes (Fig. 2a). The reflectivity in the convective core was approximately 50 dBZ. The entire system moved towards the east, and the east

convective cloud moved to the sea after 06:00 (Fig. 2c). The intensity of the storm remained similar between 02:00 and 06:00, while the scale of these two convections slightly increased during the eastward propagation. The storm left the continent and

115 continued on the sea after 08:00, Nov. 28th (not shown).
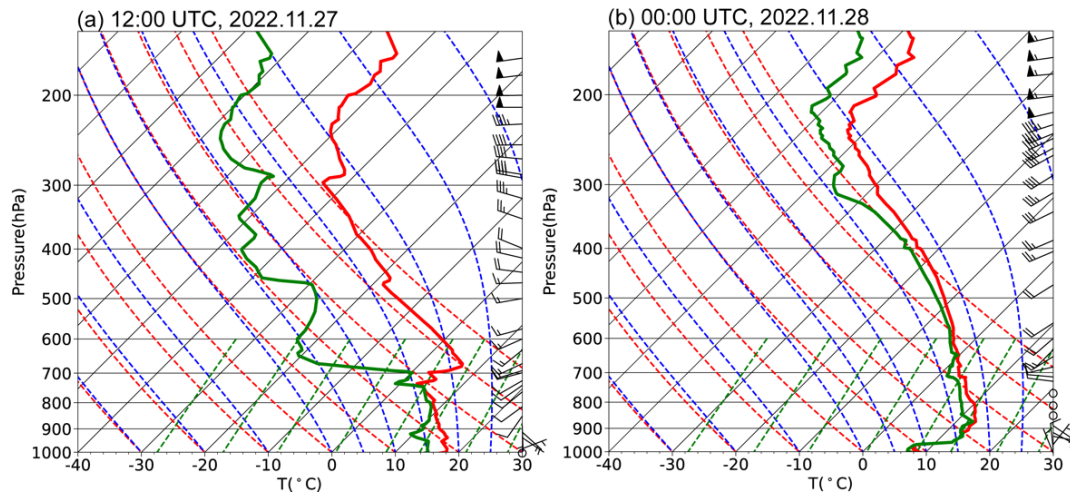
Figure 2: Skew-T log-p diagrams of sounding data from Fuyang at 12:00 UTC on Nov. 27th, and 00:00 UTC on Nov. 28th, 2022. The red profiles indicate the temperature and the green profiles indicate the dew point.
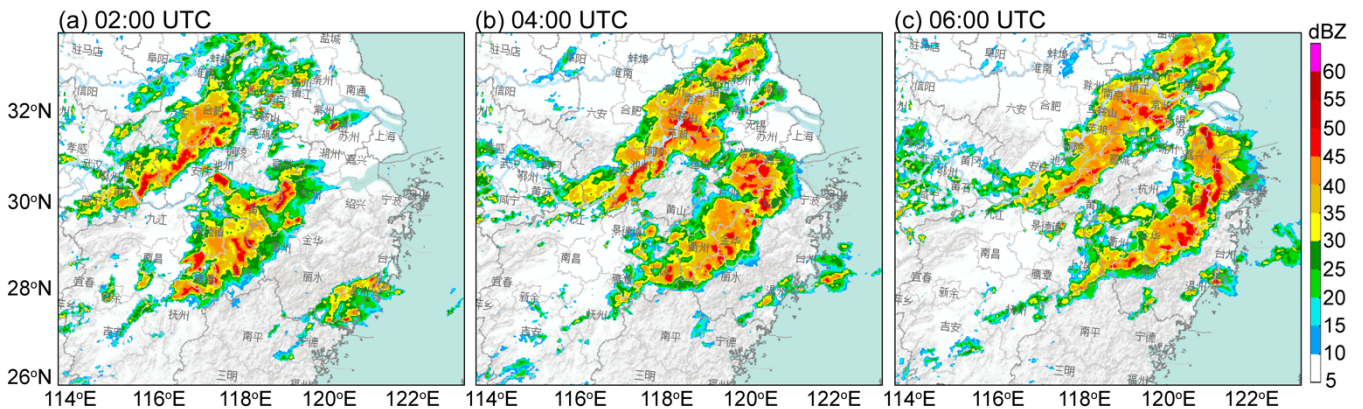
120

Figure 3: Observed radar composite reflectivity at (a) 02:00 UTC, (b) 04:00 UTC, and (c) 06:00 UTC on Nov. 28th, 2022.

2.2 Model setup and design of numerical experiments

In this simulation, two-way nested domain is used (Figure 3). The outer domain has a spatial resolution of 9 km. The resolution

125 of inner domain is 3 km, with 328 × 298 grids. There are 61 vertical levels with a top pressure of 50 hPa (~20 km). The 6-hourly NCEP FNL reanalysis data, which has a resolution of 0.25° × 0.25°, is used to drive the model and provide the boundary

condition. The simulation runs from 00:00, Nov. 27th to 12:00, Nov. 28th, with a spin up time of 12 hours. The fast SBM, in which aerosol and all the hydrometeor species are represented by 33 mass doubling bins, is used to model the cloud microphysics. The Kain-Fritsch cumulus scheme is used for the outer domain, while turned off for the inner domain. The other
130   physical choices include the Rapid Radiative Transfer Model for shortwave and longwave radiation (Mlawer et al., 1997), the Revised MM5 surface layer scheme (Jiménez et al., 2012), the Noah land surface model (Tewari et al., 2004), and the Yonsei University planetary boundary layer scheme (Hong et al., 2006).
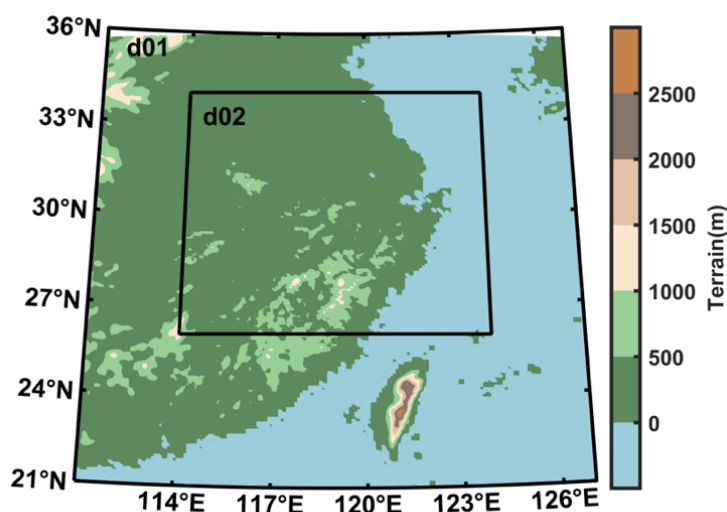
Figure 4: Domains of WRF model simulation.

135

Parameterizations of three SIP mechanisms are implemented in the SBM: the rime-splintering, ice-ice collisional breakup, and shattering of freezing drops. The equations of them are detailed in Appendix A. The parametrization of rime-splintering is developed based on the laboratory experiments made by Hallett and Mossop (1974), which shows an ice splinter is created for every 200 droplets collected by a graupel through riming at -5 °C. This SIP rate decreases as the temperature increases or
140   decreases from -5 °C. At temperature colder than -8 °C or warmer than -3 °C. The rime-splintering is inactive. The parameterization of shattering of freezing drops is also developed based on previous laboratory experiments (King and Fletcher, 1973; Philips et al., 2018). It is a set of functions depending on the particle size and temperature. In this mechanism, either tiny or big ice fragments can be produced when a supercooled liquid drop collides with an ice crystal. The production rate of ice fragments is the highest at -15 °C, but it can also active at colder and warmer temperatures (Lauber et al., 2018). The
145   parameterization of ice-ice collisional breakup is developed based on the principle of energy conservation as well as previous laboratory experiments (Takahashi et al., 1995; Yano and Phillips, 2011; Philips et al., 2017). The production rate depends on the density and shape of ice particles, as well as the collision kinetic energy.

Similar to many previous studies (Mansell, 2010; Fierro et al., 2013; Guo et al., 2017), we use the parametrization of noninductive charging developed by Saunders and Peck (1998) to simulate the cloud electrification, which is a function of particle terminal velocity, collisional efficiency, temperature and riming accretion rate (RAR). This parametrization is supported by a series of laboratory experiments demonstrating that collision between riming graupel and ice are the key noninductive charging mechanism (e.g., Brooks et al., 1997; Takahashi and Miyawaki, 2002; Saunders and Peck, 1998; Saunders et al., 2001; Emersic and Saunders, 2010). Some modelling studies showed this parameterization would result in inverted charge structure (e.g., Mansell, 2010; Phillips et al., 2020) in thunderstorm, while in this study, we will show that with SIP implemented in the model, the charge structure changes from inverted to normal, suggesting correct representative of ice generation is vital in modelling the cloud electrification. In addition, a parametrization of inductive charging (Mansell et al., 2005) is implemented in the SBM. The charge transfer occurs during riming process between polarized supercooled droplets and graupel along grazing trajectories (Moore, 1975). With charge density modelled, the electric field can be calculated based on the Poisson equation, and the discharging is simulated using a bulk model (Fierro et al., 2013). The equations of these parametrizations can be found in Appendix B.

Five sensitivity experiments are designed to investigate the impacts of different SIP processes on the cloud electrification. In the first experiment, none of the SIP parametrizations is used (hereafter noSIP); in the second experiment, only rime-splintering is considered (hereafter RS); in the third experiment, only ice-ice collisional breakup is used (hereafter IC); in the fourth experiment, only shattering of freezing drops is turned on (hereafter SD); in the last experiment, all the three SIP mechanisms are considered (hereafter 3SIP).

3 Results

3.1 Model validation

The composite radar reflectivity modelled in the five numerical experiments is shown in Figure 5. It is within expectation that the simulated convection inevitably deviates from the observed to some extent (Fig. 3), but in general, the model well captures the location and scale of the storm. The model also successfully simulates the east propagation of the storm (Fig. 5a, f, k). The SIP processes have minor impacts on the macro-properties of the storm, while the intensity can be clearly affected. At 02:00 on Nov. 28th, the noSIP experiment overestimates the composite radar reflectivity, the modelled area with reflectivity greater than 45 dBZ is much larger than observed (Fig. 3a and 5a). The IC experiment shows little improvement as the radar reflectivity is also overestimated (Fig. 5c). With rime-splintering or shattering of freezing drops considered, the modelled radar reflectivity is reduced (Figs. 5b and d), and with all the three SIP processes implemented, the simulation result is more consistent with the observation (Fig. 5e). Similarly, at 04:00, the radar reflectivity is overestimated in the noSIP experiment (Fig. 5f), and can be slightly reduced by the rime-splintering or shattering of freezing drop (Figs. 5g and i). The ice-ice collisional break up has little impact (Fig. 5h), and the simulation with all the three SIP processes has the best performance comparing to the observation

(Figs. 3b and 5j). At 06:00, the noSIP experiment again overestimates the intensity of the storm (Fig. 5k). The modelled reflectivity can be slightly improved by each of the three SIP processes (Figs. 5l, m and n), and with all the three SIP processes considered together, the simulation result is more consistent with the observation than that without SIP, not only for the intensity but also for the shape of the east convective cloud (Figs. 3c, 5k and 5o). The good performance of WRF in modelling

185   the composite reflectivity and the improvements by SIP provide us confidence to investigate the impacts of SIP on the cloud microphysics and electrification in the cold-season storm.
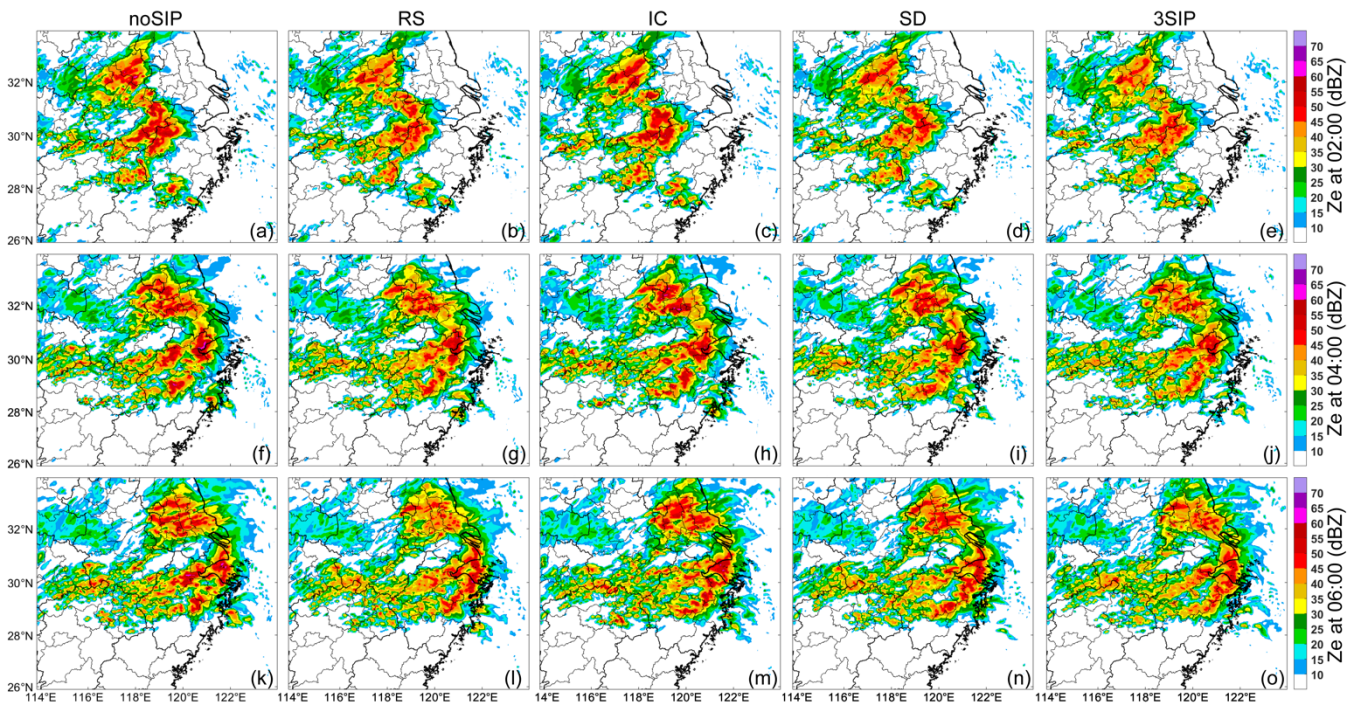
Figure 5: (a-c) Composite radar reflectivity modelled in the numerical experiment without any SIP process at 02:00, 04:00 and 06:00 UTC on Nov. 28th, 2022. (d-f) Same as (a-c) but for the experiment in which only rime-splintering is
190   **considered. (g-i) Same as (a-c) but for the experiment in which only ice-ice collisional breakup is considered. (j-l) Same as (a-c) but for the experiment in which only shattering of freezing drops is considered. (m-o) Same as (a-c) but for the experiment in which all the three SIP processes are considered.**

The flash rate from observation and the numerical experiments are compared in Figure 6. The lighting observational dataset is
195   obtained from the long-range lightning location network in China developed by Nanjing University of Information Science and Technology (Li et al., 2022). Since we use a bulk discharge model in simulating the flash, it is within expectation that there are uncertainties in modelling the lightning frequency. In addition, the lighting occurrence is strongly related to the convective cores, the uncertainty in modelling the flash rate is associated with the uncertainty in modelling the radar reflectivity (Fig. 5). However, it is seen from the figure that there is improvement in modelling the temporal variation of flash rate by

200   implementing SIP processes. The observation indicates the highest flash rate occurred between 00:00 and 01:00, Nov. 28th.
      Without any SIP, the flash rate is relatively high before 00:00, Nov. 28th. The ice-ice collisional break up enhances the flash
      rate but does not change the temporal variation. The rime-splintering and shattering of freezing drop can improve the simulation
      as the modelled flash rate is reduced before 00:00, Nov. 28th and enhanced after 00:00, Nov. 28th, which is more consistent
      with observation. With all the three SIP processes implement, the flash rate after 00:00, Nov. 28th is further enhanced, and the
205   modelled result is more consistent with the observation than the other experiments. This provides the basis for further analyzing
      the cloud electrification.
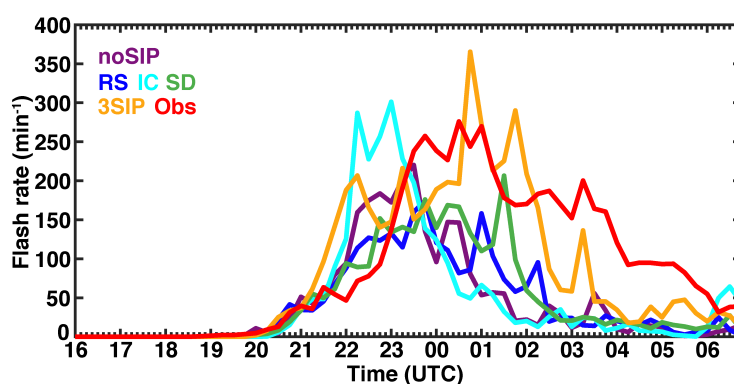
Figure 6: Flash rate in the inner domain of the model obtained from observation and the numerical experiments from 16:00, Nov. 27th to 06:30, Nov. 28th, 2022.

210

3.2 The impact of ice multiplication on cloud microphysics

The charge structure in thunderstorm is controlled by the microphysics. Figure 7 presents the time-height diagrams of the mixing ratio of graupel/hail, ice/snow, rain and cloud water in different experiments. It is seen from the figure that the modelled convection was weak before 18:00, Nov. 27th, and only warm rain was present. Between 18:00 and 20:00, the storm rapidly

215   intensified, and the cloud mixing ratio increased substantially. The modelled cloud top reached approximately 12 km above the mean sea level (a.m.s.l.). Between 22:00, Nov. 27th and 02:00, Nov. 28th, the surface rain was relatively strong, and the maximum graupel and rain mixing ratio were about 7 g ks^{-1} and 8 g kg^{-1}. The snow mixing ratio was lower than that of graupel and rain in this period. The strong correlation between the graupel and rain water mixing indicate the melting of graupel had great contribute to the rainfall. After 01:00, Nov. 28th, the cloud top decreased, the surface rain was weakened, and the graupel

220   and liquid water mixing ratio decreased (Fig. 7a and p), suggesting weakening convective updrafts, and this results in the declining flash rate after 01:00 (Fig. 6). However, the snow mixing ratio was higher than that before 02:00, exceeding the mixing ratio of graupel, suggesting melting of snow might be more important to the rainfall in this period.

The rime-splintering process has a clear enhancing effect on the graupel mixing ratio between 22:00, Nov. 27th and 02:00, Nov. 28th (Fig. 7b), and snow mixing ratio after 02:00, Nov. 28th (Fig. 7g). The enhancement of graupel mixing is found mainly above 6 km, while rime-splintering is mainly active between -3 °C and -8 °C, which is below 6 km. This indicates the secondary ice particles might transport to upper levels in the convection. However, the rain mixing ratio decreases due to the SIP by rime-splintering, suggesting less graupel falling out of the cloud, this is probably due to the smaller size of graupel (shown later). The ice-ice collisional breakup also enhances the graupel mixing ratio before 02:00, Nov. 28th and snow mixing ratio after 02:00, Nov. 28th. In addition, the rain and cloud water mixing ratio are also enhanced, especially at 4 km (Fig. 7m) and 7 km (Fig. 7r), respectively. The shattering of freezing drops has a minor impact on the graupel mixing ratio (Fig. 7d), however, this does not mean there is few secondary ice particles produced, in fact, the concentration of graupel is enhanced while the size is reduced by this SIP (shown later). The snow mixing ratio is enhanced due to shattering of freezing drops after 02:00, Nov. 28th (Fig. 7i) and the rain mixing ratio is reduced before 02:00, Nov. 28th (Fig. 7n), With all the three SIP processes implemented, the graupel mixing is slightly enhanced, and the snow mixing ratio is enhanced as well. However, the rain mixing ratio is reduced, resulting slightly weaker surface precipitation.
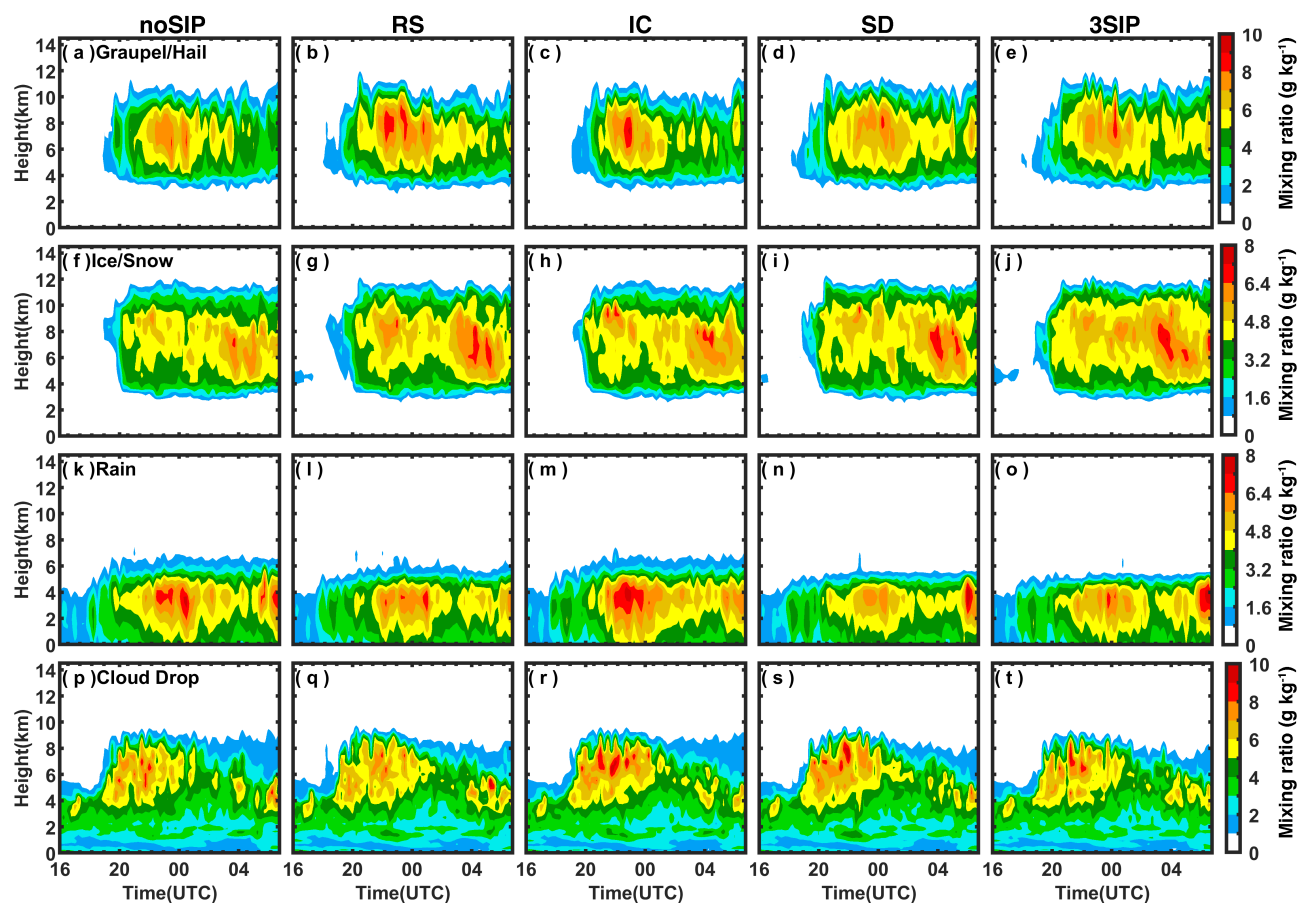
Figure 7: Time-height diagrams of the mixing ratio of (a-d) graupel/hail, (e-h) ice/snow, (i-l) rain and (m-p) cloud droplets from the four simulations. (a, e, i, m) SBM-0SIP Simulation; (b, f, j, n) SBM-1SIP Simulation; (c, g, k, o) SBM-2SIP Simulation; (d, h, l, p) SBM-3SIP Simulation.

Figure 8 shows the temporal variation of the mean concentrations and sizes of graupel/hail, ice/snow and rain, respectively. It is seen that the graupel and ice concentration was very low (larger than 0) before 20:00, Nov. 27th as the cloud top was low, while the average size of graupel was the largest at 19:00. After 20:00, Nov. 27th, the concentrations of the hydrometeors quicky increased as the storm intensified. The SIP by rime-splintering and shattering of freezing drops can enhance the graupel concentration while suppress their sizes. The ice-ice collisional breakup has minor impacts on the graupel properties on average. The ice/snow concentration is slightly enhanced by ice-ice collisional breakup and shattering of freezing drops, while if all the three SIP processes work together, the ice/snow concentration is clearly higher than that without SIP, and the ice/snow size is reduced after 00:00, Nov. 28th. The rain concentration also slightly decreases due to the three SIP processes, while the impacts of SIP on the average cloud droplet concentration and size are very minor (not shown). According to Figs. 7 and 8, it is evident that the graupel and snow microphysics can be strongly affected by the SIP, and the decrease in the sizes of these solid particles is probably the main reason of the weaker composite radar reflectivity in the 3SIP experiment (Fig. 5).
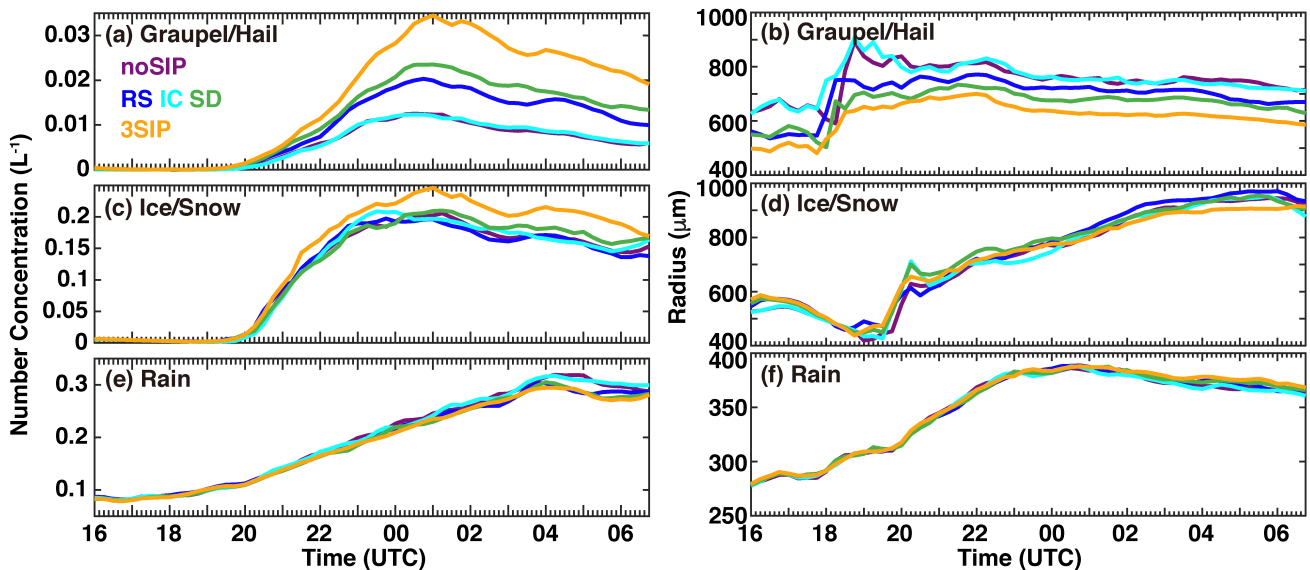
Figure 8: Temporal variation of the average concentrations (left panels) and sizes (right panels) of (a, b) graupel/hail, (c, d) ice/snow, and (e, f) rain.

3.2 The impact of ice multiplication on cloud electrification

The enhanced graupel and ice mixing ratio and concentration would affect the charging rate by enhancing the graupel-ice collision and riming process. Figure 9 shows the average noninductive and inductive charging rate obtained from the five
260 numerical experiments. Note the charging rate averaged over the model domain is very small, the maximum charging rate (not shown) is more than 4 orders of magnitudes larger than the average value, but the pattern is similar, thus providing the same conclusions. It is seen from the figure that the cloud electrification starts at about 19:00, Nov. 27th. Without any SIP considered in the model, the noninductive charging rate has an obvious separation at -20 °C, with negative charging above this level, and positive charging below (Fig. 9a). The magnitude of the upper-level negative charging rate is slightly larger than the positive
265 charging rate. However, with rime-splintering included, the positive charging rate below 7 km is clearly enhanced (Fig. 9c), as rime-splintering is efficient at relatively warm temperature. In fact, rime-splintering process is mainly efficient between -3 °C and -8 °C, but the secondary ice can transport to higher levels in convection. The shattering of freezing drops also enhances the positive charging rate below 7 km (Fig. 9g), this SIP is more efficient than the rime-splintering at temperatures colder than -8 °C. The ice-ice collisional breakup can slightly enhance the graupel and ice mixing ratio, but its impact is too weak to
270 modify the charging rate in this case (Fig. 9e). With all the three SIP processes included, the low-level positive noninductive charging rate on graupel is clearly enhanced (Fig. 9i), mainly due to the composite impact of rime-splintering and shattering of freezing drops. The magnitude of upper-level negative noninductive charging rate remains similar compared to that without SIP. The inductive charging rate is a few times smaller than the noninductive charging rate, but cannot be neglected. The rime-splintering and shattering of freezing drops result in very different structures of the inductive charging rate compared to that
275 without SIP (Fig. 9b, d, h). The upper-level negative charging on graupel in noSIP experiment is changed to positive, this implies that the total charge structure may be inverted above 6 km due to these two SIP processes, which will be demonstrated later. With all the three SIP processes implemented, the inductive charging on graupel is positive at most of the levels (Fig. 9j), while at about -10 °C, the graupel sometimes gets negative charging. This indicates an opposite sign of vertical electric field; thus, positive charge (or relatively weak negative charge) regions are present at some locations at this level.

280

The modified charging rate by SIP result in changes in the structure of charge density carried by different hydrometeors, especially the graupel and ice. As shown in Figure 10, the average charge density carried by graupel/hail is negative at all levels if not considering the SIP. Although the graupel gets positive charge by colliding with ice below 8 km (Fig. 9a), the graupel falling from upper levels brings negative charge to the lower levels. In addition, the graupel may get negative charge
285 through riming (Fig. 9b). Therefore, the composite negative charge on graupel exceeds the positive charge generated by noninductive charging. The ice/snow mainly carries positive charge below 10 km (Fig. 10f), indicating significant sedimentation of snow crystals generated between 8 km and 10 km, and the positive charge carried by these falling snow crystals exceeds the negative charge transferred to snow through noninductive charging below 8 km. The enhanced noninductive charging rate by rime-splintering resulting in positive (negative) charge on graupel (snow) below 7 km (Fig. 10

b and g), indicating the positive charge on graupel gained from charge separation at this level exceeds the negative charge

290 carried by the falling graupel. In addition, the upper-level negative charge on graupel is weakened due to the positive inductive charging (Fig. 9d). The shattering of freezing drops has similar impact on the charge structure compared to rime-splintering, but the region with the most enhancement of the positive charge on graupel is slightly higher in SD experiment than in RS experiment (Fig. 10d and i), because the rime-splintering is active between -3 °C and -8 °C, while shattering of freezing drops

295 is also active at colder temperatures. Above 7 km, the negative charge carried by graupel is weakened, probably due to the enhanced positively inductive charging (Fig. 9d and h). The composite effect of rime-splintering and shattering of freezing drops result in a strong positive (negative) charge region on graupel (snow) below 8 km, and the top positive (negative) charge region on graupel (snow) is significantly weakened (Fig. 9e and j).
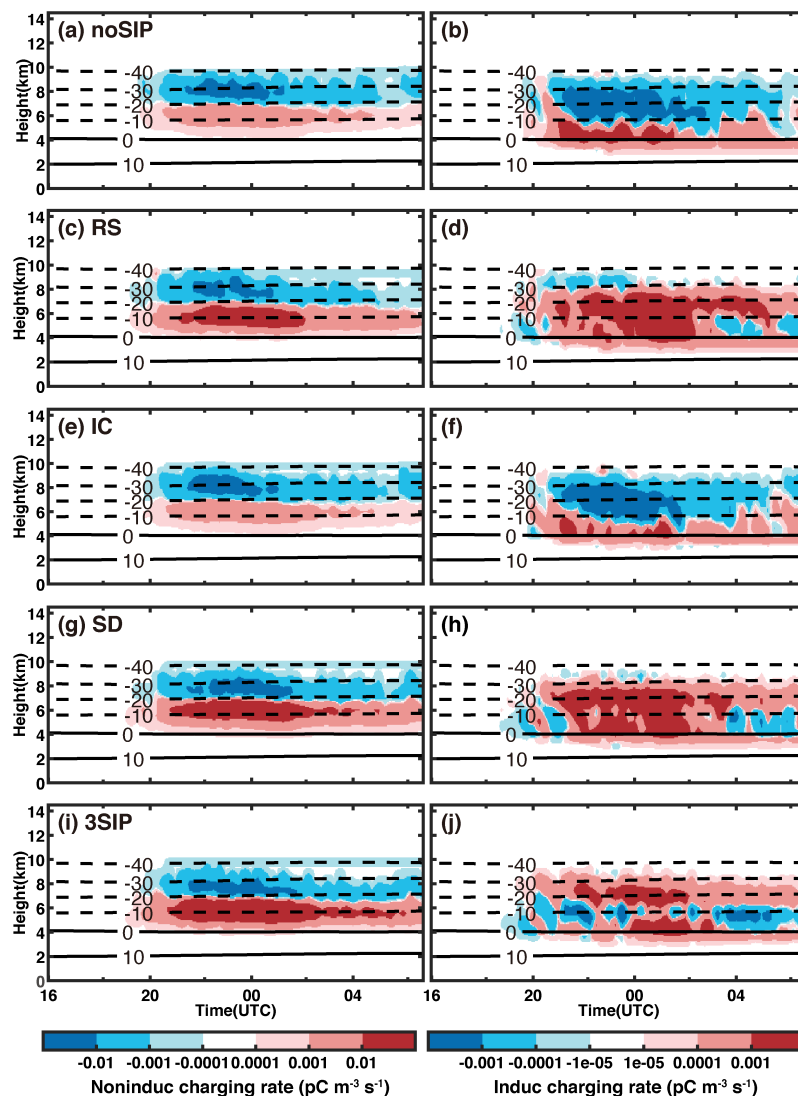
300   **Figure 9: Time-height diagrams of the charging rate on graupel through noninductive (left panels) and inductive (right panels) charging from the five experiments. (a, b) experiment without SIP, (c, d) experiment with rime-splintering, (e, f) experiment with ice-ice collisional breakup, (g, h) experiment with shattering of freezing drops, and (i, j) experiment with three SIP processes. The black contours are the isotherms.**
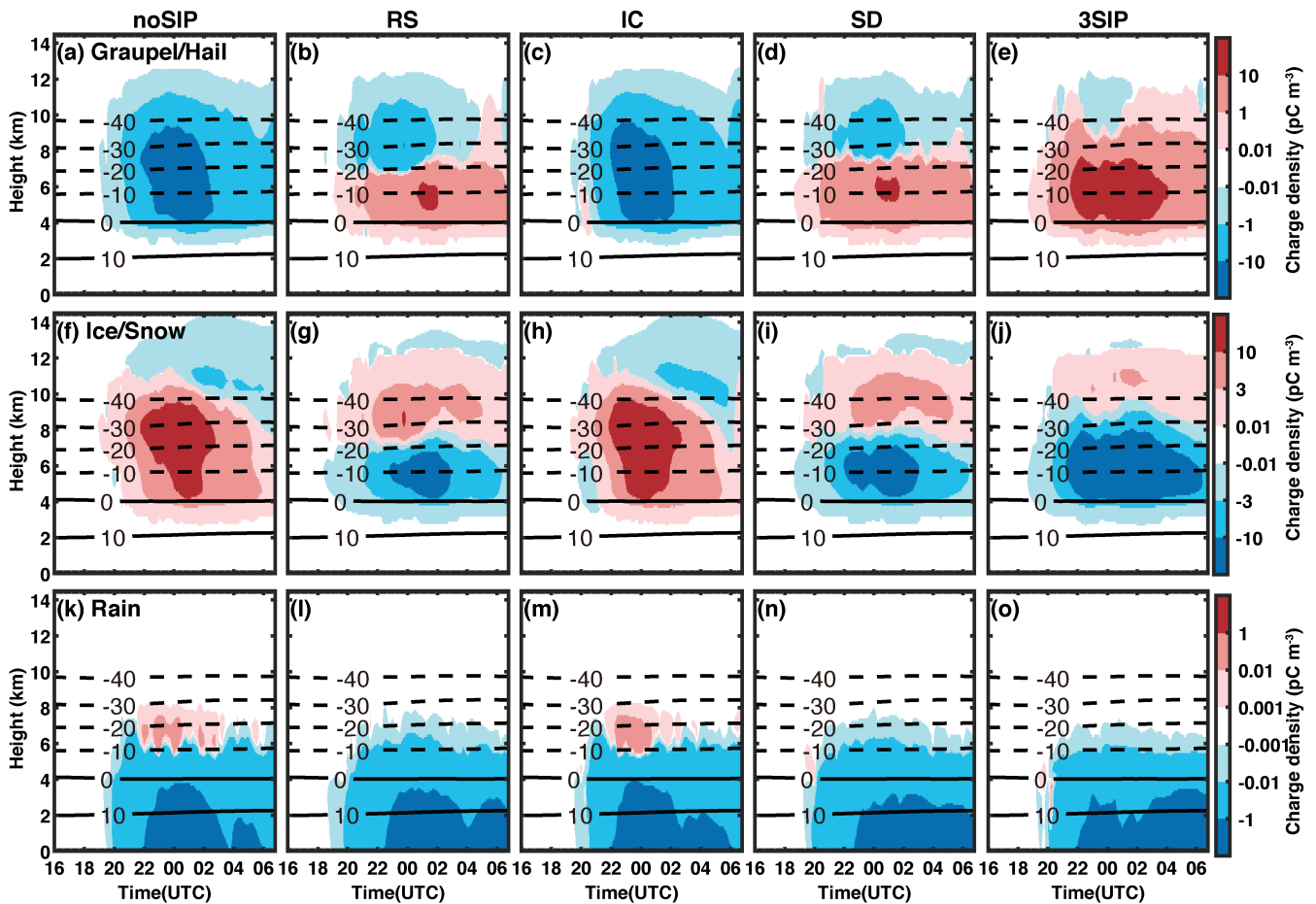
305

Figure 10: Time-height diagrams of the charge density carried by (a-e) graupel/hail, (d-j) ice/snow, and (k-o) rain from the five simulations. (a, f, k) experiment without SIP, (b, g, l) experiment with rime-splintering, (c, h, m) experiment with ice-ice collisional breakup, (d, i, n) experiment with shattering of freezing drops, and (e, j, o) experiment with three SIP processes. The black contours are the isotherms.

310

The time-height evolution of the total charge density obtained from different simulations is shown in Figure 11. In the experiment without any SIP (Fig. 11a), the storm has an inverted tripole structure with a positive charge region at 7-10 km, and an upper and a lower negative charge region. The positive charge region weakened after 02:00, Nov.28th due to the lower

positive charging rate (Fig. 9a). The ice-ice collisional breakup may slightly enhance the positive charge region (Fig. 11c), but

315 this impact is minor as its impact on the ice microphysics and charging rate are weak (Figs. 7 and 9e). With either rime-splintering or shattering of freezing drops implemented, the charge density changes to a dipole structure on average (Fig. 11b and d). Positive charge dominated above 7 km, while negative charge dominated below 7 km, though the magnitude is small. This indicate the magnitude of charge carried by ice/snow is slightly larger than the that carried by graupel/hail (Fig. 10b, d, g, and i). With the three SIP processes included, the charge structure is dipole as well, suggesting the rime-splintering and

320 shattering of freezing drops dominate the SIP effect. In addition, it is seen that the charge reversal level shifts upwards by about 1 km and the magnitude of the upper-level positive charge density is lower compared to that in RS and SD experiments due to the composite effect of the SIP.
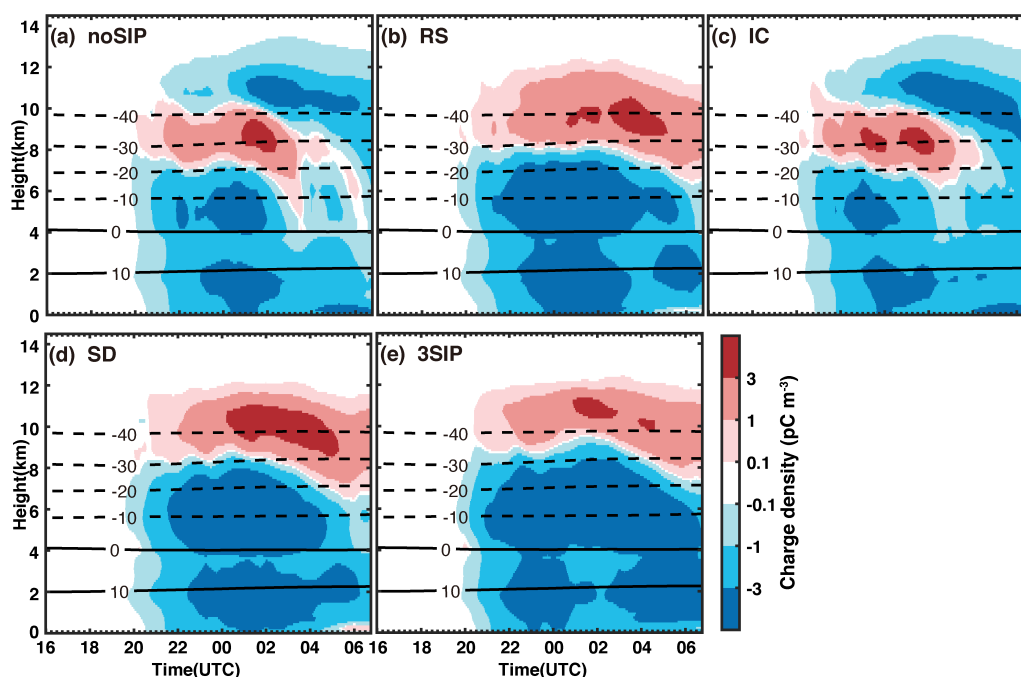
Figure 11: Time-height diagrams of the total charge density (colored) and temperature (contours) from the five

325 **numerical experiments. (a) experiment without SIP, (b) experiment with rime-splintering, (c) experiment with ice-ice collisional breakup, (d) experiment with shattering of freezing drops, and (e) experiment with three SIP processes.**

The structure of the average charge density shown Fig. 11 looks fairly simple, however, the actual charge structure along a given cross section is complicated, and it may change rapidly with time. Figure 12 shows the cross section of the total charge

330 density along 118°E, 30°N – 121°E, 30°N. In general, if no SIP is considered, there is a main upper negative and a main middle positive charge region, a weak negative charge region is observed sometimes at the bottom of the cloud. But the charge structure could be different at different locations, suggesting complicated microphysics processes. The rime-splintering and shattering of freezing drops both result in a main upper positive and a main lower negative charge region in the storm, but the

charge structures vary significantly along the cross section, such as that between 0 km and 50 km, and that between 50 km and
335   200 km in Figs. 12b, g and i. With all the SIP processes considered, the storm obtains an opposite charge structure compared
to that in noSIP experiment, as there is a main positive charge region at the top and a main middle negative charge region.
Weak positive charge region is present at some locations near 0 °C, this is probably the reason for the negative inductive
charging rate on graupel at -10 °C (Fig. 9j), but it cannot be intuitively revealed after averaging (Fig. 11e). The substantial
change in the charge structure induced by SIP suggesting the charge separation in this storm is very sensitive to the ice and
340   graupel generation (i.e., increase in ice and graupel mixing ratio and number concentration).
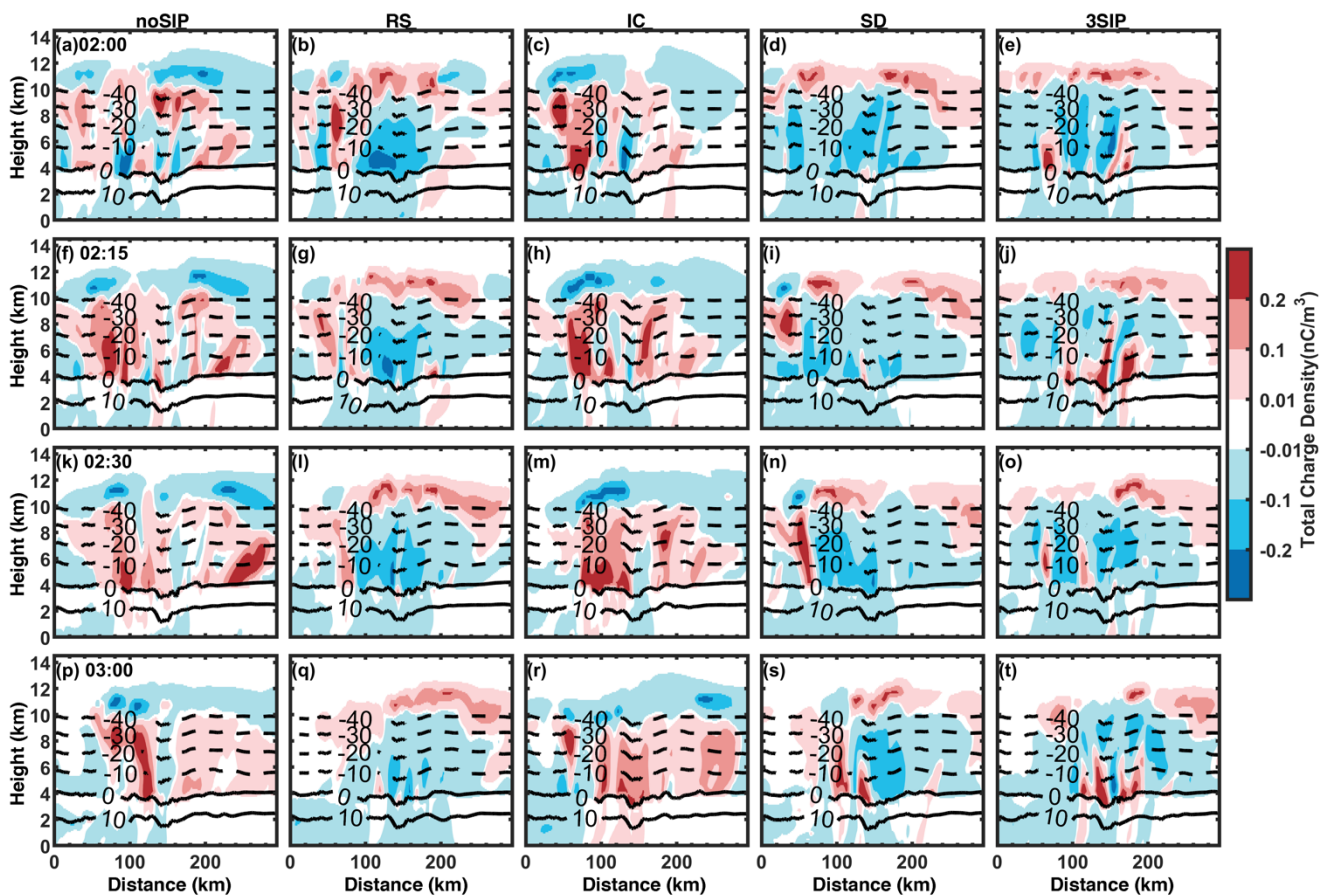
**Figure 12: Cross sections of the modelled total charge density at different times from the five numerical experiments.
(a, f, k, p) experiment without SIP, (b, g, l, q) experiment with rime-splintering, (c, h, m, r) experiment with ice-ice
collisional breakup, (d, i, n, s) experiment with shattering of freezing drops, and (e, j, o, t) experiment with three SIP
345   processes.**

Changes in the structure of total charge density result in changes in the electric field by the SIP. Figure 13 shows the time-height diagram of the vertical electric field modelled in different experiments, it is evident that the electric field is enhanced by the SIP, especially by the rime-splintering and shattering of freezing drops. The changes in the electric field explains the

350 temporal variation of lightning frequency in Fig. 6. If considering the ice-ice collisional breakup only, the electric field is enhanced between 22:00, Nov. 27th and 00:00, Nov. 28th (Fig. 13c), resulting in higher lightning frequency in this period. The rime-splintering and shattering of freezing drops enhance the vertical electric field after 00:00, Nov. 28th (Fig. 13b and d), therefore, the lightning frequency after that time is as high as that before, this is different from that in the noSIP and IC experiment, in which the lightning frequency rapidly decreased after 00:00, Nov. 28th. With all the three SIP processes

355 implemented, the eclectic field is clearly enhanced, especially after 00:00, Nov. 28th (Fig. 13e), resulting in higher lightning frequency in the entire period.
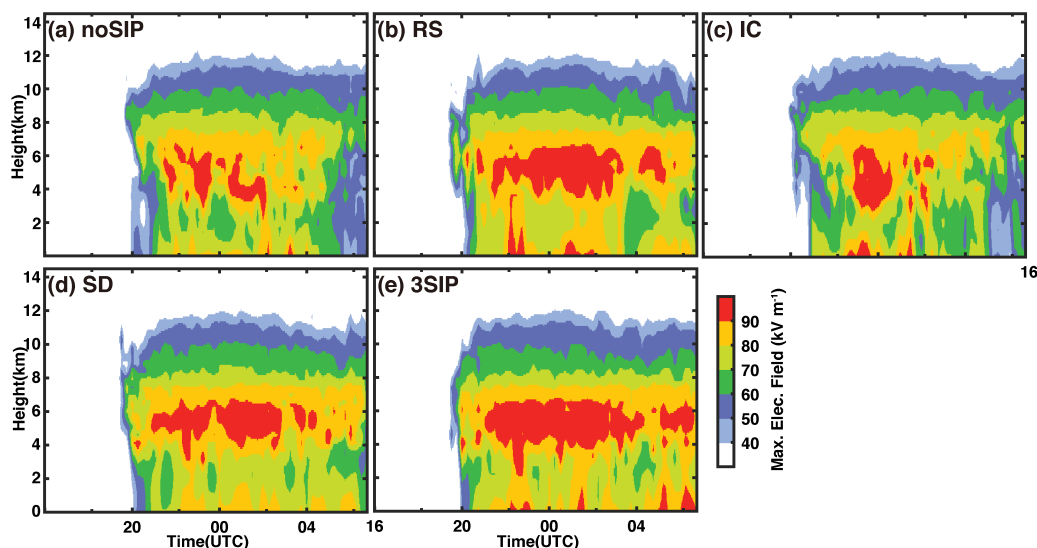
Figure 13: Time-height diagrams of the maximum vertical electric field from the five numerical experiments. (a) experiment without SIP, (b) experiment with rime-splintering, (c) experiment with ice-ice collisional breakup, (d)

360 **experiment with shattering of freezing drops, and (e) experiment with three SIP processes.**

5 Discussion and Conclusions

In this study, the impacts of different SIP processes on the cloud electrification in a cold-season thunderstorm is investigated using WRF model simulations with SBM microphysics scheme. The storm occurred in late November in southeast China. Three SIP processes are considered in the model, including the rime-splintering, the ice-ice collisional breakup, and shattering

365 of freezing drops. In addition, a noninductive and an inductive charging parametrization, as well as a bulk discharging model are coupled with the SBM microphysics. The impacts of different SIP processes on the cloud microphysics and electrification are compared using five sensitivity experiments, one control run without SIP, one with all the three SIP processes, and three

in each a single SIP is used. The results contribute to fill the dearth of understanding the impact of different SIP processes on the cloud electrification in cold-season thunderstorms.

370

Comparison between model simulation and observation suggest the model well captures the scale and east propagation of the storm. The SIP has minor impacts on the macro-properties of the storm, while the intensity can be affected. If no SIP is considered, the model overestimates the composite radar reflectivity. The ice-ice collisional breakup has minor impacts on the radar reflectivity, while if rime-splintering or shattering of freezing drops is used, the modelled radar reflectivity is reduced.

375 With all the three SIP processes implemented, the simulation result is more consistent with the observation. This is mainly because the SIP processes suppress the sizes of graupel and snow, though their concentration can be enhanced. The implementation of SIP also improves the simulation of flash rate. Without any SIP, the peak flash rate is obtained earlier than observed. The ice-ice collisional break up enhances the flash rate but does not change the temporal variation. The rime-splintering and shattering of freezing drop can improve the temporal variability of flash rate. With all the three SIP processes

380 implement, both the temporal variation and magnitude of the flash rate are more consistent with the observation.

The enhanced graupel and ice mixing ratio and concentration would affect the charging rate by enhancing the collision between graupel and ice, as well as the riming process. In the case presented in this paper, the noninductive charging rate has a reversal at -20 °C, with negative charging on graupel above this level, and positive charging below. Without SIP considered, the

385 magnitude of the upper-level negative charging rate is slightly larger than the positive charging rate. With rime-splintering or shattering of freezing drops included, the positive charging rate is substantially enhanced. The inductive charging rate is a few times smaller the noninductive charging rate, and the SIP can change the upper-level inductive charging on graupel from negative to positive. The changes in the charging rate due to SIP result in substantial modification of the charge structure. The charge density carried by graupel and snow below -20 °C obtain an opposite sign after SIP is implemented in the model. The

390 total charge density changes from an inverted tripole structure to a dipole structure (tripole structure at some locations) after SIP is implemented in the model. These changes lead to an enhancement of vertical electric field, especially in the mature stage, which explains the improved temporal variation of flash rate in the model.

The ambient temperature near surface in this cold-season storm is approximately 10 °C lower than that in summer. In many

395 previous studies of summertime thunderstorm occurred at a similar latitude (e.g., Caicedo et al., 2018; Shi et al., 2015), the main charging region is typically at 5-11 km a.m.s.l., and the freezing level is at about 5 km a.m.s.l, which are all about 1 km higher than the cold-season storm shown in this paper. The implementation of SIP would further enhance the low-level charging in cold-season conditions. Therefore, the height of flash initiation is expected to be lower in cold-season than that in warm season.

400

Observational studies suggest there are a variety of charge structures in different thunderstorms (Qie et al., 2019). Unfortunately, we do not have charge measurement in this case, so we are not able to evaluate the modelled charge structure. But the result in the simulation with three SIP processes is consistent with many observational studies of cold-season thunderstorm, though occurred in different regions (e.g., Kitagawa and Michimoto, 1994; Takahashi et al., 1999, 2018, 2019; Yoshida et al., 2018; Zheng et al., 2018). Takahashi et al. (1999, 2018) investigated the evolution of charge structure in Hokuriku winter thunderstorms, and they suggested that the charge separation of graupel is observed at -10 °C. Graupel embryos forms at temperatures lower than -10 °C, and continued growing through riming. The graupel gets negative charging when it collides with ice crystals at temperatures colder than -10 °C. While it gets positive charging if falling to levels warmer than -10 °C. This result is consistent with our finding, except that the sign of charging on graupel reversed at -20 °C in the present study.

Some studies suggested the charge separation in thunderstorm is sensitive to the parametrization of electrification (Altaratz et al., 2005; Fierro et al., 2013; Xu et al., 2019). Here, we highlight that the cold-season cloud electrification is also sensitive to the SIP. However, the results shown here only reveal the relative importance of three SIP mechanisms on a single case. While in other cases, the SIP processes may have different impacts on the charge structure. For example, Phillips and Patade (2022) suggested in summertime thunderstorms with high cloud base, the ice-ice collisional breakup has stronger impacts than the other SIP mechanisms, which is different from the result shown in this paper. This indicates factors such as the dynamics and thermodynamics of storms may control the role of SIP in thunderstorms. In addition, only three SIP mechanisms are implemented in the model in this study, because these SIP processes are important in convective clouds and there are observational datasets available for developing the parameterizations. Some other SIP mechanisms may also contribute to the ice generation, such as the breakup of snow during sublimation, and ice fragmentation due to thermal shock (Korolev et al., 2020). Furthermore, an INP may be activated at a warmer temperature if there was ice growing upon it and subsequently sublimated. Some studies suggested this so-called "pre-activation" of INPs may enhance the ice generation in mixed-phase clouds by more than 260% at -10 °C (Jing et al., 2022). It is worth investigating the impacts of these mechanisms on the cloud microphysics and electrification using model simulations once there are sufficient measurements to support the development of parameterizations in the future.

Appendix A

Based on laboratory experiment, Hallett and Mossop (1974) showed one ice splinter can be generated during riming process for every 200 droplets collected by a graupel. The ice splinter production rate of rime-splintering N_{RS} is:

$$N_{RS} = 3.5 \cdot 10^5 \cdot \left(\frac{\partial m_g}{\partial t}\right) \cdot R_{rim}(T) \tag{A1}$$

$$R_{rim}(T) = \begin{cases} 0, & T \geq 270.16K \\ (T - 268.16)/2, & 268.16K \leq T < 270.17K \\ (T - 268.16)/3, & 265.16K \leq T < 268.16K \\ 0, & T < 265.16K \end{cases} \tag{A2}$$

where, $\frac{\partial m_g}{\partial t}$ indicates the riming rate, T is the temperature.

The parametrization of ice–ice collisional breakup is developed by Phillips et al. (2017). The number of ice fragments produced during ice–ice collision is:

$$N_{IC} = \alpha A(M) \left\{ 1 - \exp\left[-\left(\frac{C(M)K_0}{\alpha A(M)} \right)^{\gamma} \right] \right\} \tag{A3}$$

where, $A(M)$ is the number density of breakable asperities on the ice particle, $C(M)$ is asperity–fragility coefficient, K_0 is initial value of collision kinetic energy, γ and α are the shape parameter and the equivalent spherical surface area of smaller particles, respectively.

The parameterization of shattering of freezing drops is developed by Phillips et al. (2018) based on laboratory experiments. If contacting with a small ice particle, a supercooled drop may breakup and produce both big and tiny ice fragments, thus, the number of the ice fragments can be expressed using:

$$N_{SD\_1} = N_T + N_B \tag{A4}$$

$$N_T = F(D)\Omega(T) \left[\frac{\xi_T \eta_T^2}{(T - T_{T,0})^2 + \eta_t^2} + \beta T \right] \tag{A5}$$

$$N_B = \min\left\{ F(D)\Omega(T) \left[\frac{\xi_B \eta_B^2}{(T - T_{B,0})^2 + \eta_B^2} \right], N_T \right\} \tag{A6}$$

where, N_T and N_B are the number of tiny and big ice fragments generated by a shattered drop. $F(D)$ and $\Omega(T)$ are the interpolating functions for the onset of drop shattering. $\xi_T, \xi_B, \eta_T, \eta_B, T_{T,0}, T_{B,0}, \beta$, are parameters determined based on datasets from previous laboratory experiments.

In addition, a drop may also break if contacting with a more massive ice particle. The number of ice fragments produced in this process is:

$$N_{SD\_2} = 3\Phi \times [1 - f(T)] \times \max\left\{ \left(\frac{k_0}{S_e} - DE_{crit} \right), 0 \right\} \tag{A7}$$

$$f(T) = \frac{-C_w T}{L_f} \tag{A8}$$

$$S_e = \gamma_{liq} \pi D^2 \tag{A9}$$

where, γ_{liq} is the surface tension of liquid drop, k_0 is the initial kinetic energy of the two colliding particles, $f(T)$ is the frozen fraction. C_w and L_f are the specific heat capacity of water and the specific latent heat of freezing, respectively. $DE_{crit} = 0.2$,

and Φ is 0.3 according to James et al. (2021). All ice fragments are assumed to be tiny in this mode. The tiny ice fragments are added to the first bin of ice size distribution, and the mass of big ice fragments is $m_B = 0.4m_{drop}$.

460 **Appendix B**

The non-inductive charging produced during the collision between graupel and ice crystal is expressed as:

$$\frac{\partial \rho_{gi}}{\partial t} = \iint_0^\infty \frac{\pi}{4} \beta \delta q_{gi} (1 - E_{gi}) |V_g - V_i| (D_g + D_i)^2 n_g n_i dD_g dD_i \tag{B1}$$

$$\beta = \begin{cases} 1, & T > -30\,\text{°C} \\ 1 - \left[\frac{T+30}{13}\right]^2, & -43\,\text{°C} < T < -30\,\text{°C} \\ 0, & T < -43\,\text{°C} \end{cases} \tag{B2}$$

where, T is temperature. E_{gi} is collection efficiency between graupel and ice. V, D and n are the terminal velocity, diameter,
465 and number concentration, with subscripts g and i indicate graupel and ice crystals. The charge transferred per rebounding collision (δq_{xy}) is a function of RAR and critical RAR (RAR_c) (Saunders and Peck 1998):

$$\delta q_{xy} = B d^a V^b \delta q_\pm \tag{B3}$$

where, B, a and b are parameters determined based on laboratory studies. For positive charging of graupel ($\text{RAR} > \text{RAR}_c$),

$$\delta q_+ = 6.74(\text{RAR} - \text{RAR}_c) \tag{B4}$$

470 and for negative charging ($0.1 gm^{-2}s^{-1} < \text{RAR} < \text{RAR}_c$),

$$\delta q_- = 3.9(\text{RAR}_c - 0.1)\left\{4\left[\frac{\text{RAR} - (\text{RAR}_c + 0.1)/2}{\text{RAR}_c - 0.1}\right]^2 - 1\right\} \tag{B5}$$

$$\text{RAR}_c = \begin{cases} s(T), & T > -23.7\text{°C} \\ k(T), & -23.7\text{°C} > T > -40\text{°C} \\ 0, & T \le -40\text{°C} \end{cases} \tag{B6}$$

$$s(T) = 1.0 + 7.9262 \cdot 10^{-2}T + 4.4847 \cdot 10^{-2}T^2 + 7.4754 \cdot 10^{-3}T^3 + 5.4686 \cdot 10^{-4}T^4 + 1.6737 \cdot 10^{-5}T^5 + 1.7613 \cdot 10^{-7}T^6 \tag{B7}$$

475
$$k(T) = 3.4\left[1.0 - \left(\frac{|T+23.7|}{-23.7+40.0}\right)^3\right] \tag{B8}$$

According to Mansell et al. (2005), the inductive charging rate is parametrized as:

$$\frac{\partial \rho_g}{\partial t} = \left(\frac{\pi^3}{8}\right)\left(\frac{6.0\bar{V}_g}{\Gamma(4.5)}\right) E_{gc} E_r n_c n_{0g} D_c^2 \times \left[\pi\Gamma(3.5)\epsilon\langle cos\theta\rangle E_z \mathcal{D}_g^2 - \Gamma(1.5)\frac{\rho_g}{3n_g}\right] \tag{B9}$$

where, E_{gc} is the collision efficiency between graupel and droplet. E_r is the rebound probability. n_c is the number

480 concentration of cloud droplet. n_{0g} is the intercept of graupel size distribution. θ is the rebounding collision angle. ϵ is the permittivity of air. E_z is the vertical electric field, and ρ_g is the charge density carried by graupel.

The discharge model used in this paper is a bulk discharge scheme suggested by Fierro et al. (2013), in which flash occurs once the electric field exceeds a threshold. The electric field (E) can be computed by solving the Poisson equation:

485
$$\nabla^2 \emptyset = -\frac{\rho_{tot}}{\epsilon} \tag{B10}$$

$$\mathbf{E} = -\nabla \emptyset \tag{B11}$$

where, ρ_{tot} is the net charge density.

Data availability

The WRF model is available on https://www.mmm.ucar.edu/models/wrf. The reanalysis data used to drive WRF model is
490 available on https://rda.ucar.edu/datasets/ds083.2/dataaccess/. The observed radar reflectivity images, sounding data and lightning data are available on https://doi.org/ 10.5281/zenodo.8371845.

Author contributions

SH and JY implemented the parametrizations of SIP and electrification in WRF, and designed the numerical experiments. SH, JY, and YL performed the analysis and prepared the manuscript. QZ and YD contribute to the model evaluation. QZ and XJ
495 provided input on the method and analysis. All authors provided significant feedback on the manuscript.

Competing interests

The contact author has declared that none of the authors has any competing interests.

Acknowledgements

This work was supported the National Key R&D Program of China (Grant No. 2023YFC3000067), the National Natural
500 Science Foundation of China (41905124), the Natural Science Foundation of Jiangsu Province, China (BK20190778), and the CMA Key Innovation Team Support Project (CMA2022ZD10). We appreciate the editor and reviewers for their insightful comments and suggestions.

References

Altaratz, O., Reisin, T. and Levin, Z.: Simulation of the electrification of winter thunderclouds using the three-dimensional regional atmospheric modeling system (RAMS) model: Single cloud simulations. Journal of Geophysical Research: Atmospheres, 110, D20, doi: 10.1029/2004JD005616, 2005.

Baker, M. B., Christian, H. J., and Latham, J.: A computational study of the relationships linking lightning frequency and other thundercloud parameters. Quarterly Journal of the Royal Meteorological Society, 121, 1525–1548, doi: 10.1002/qj.49712152703, 1995.

Brook, M.: Breakdown electric fields in winter storms. Journal of Atmospheric Electricity, 12, 47-52, doi: 10.1541/jae.12.47, 1992.

Brooks, M. I., Saunders, C. P. R., Mitzeva, R. P., and Peck, S. L.: The effect on thunderstorm charging of the rate of rime accretion by graupel. Atmos. Res., 43, 277–295, doi: 10.1175/MWR-D-12-00278.1, 1997.

Caicedo, J. A., Uman, M. A., and Pilkey, J. T.: Lightning evolution in two North Central Florida summer multicell storms and three winter/spring frontal storms. Journal of Geophysical Research: Atmospheres, 123, 1155–1178, doi: https://doi.org/10.1002/2017JD026536, 2018.

Emersic, C., and Saunders, C. P. R.: Further laboratory investigations into the relative diffusional growth rate theory of thunderstorm electrification. Atmos. Res., 98, 327–340, doi: 10.1016/j.atmosres.2010.07.011, 2010.

Fierro, A. O., Mansell, E. R., MacGorman, D. R., and Ziegler, C. L.: The Implementation of an Explicit Charging and Discharge Lightning Scheme within the WRF-ARW Model: Benchmark Simulations of a Continental Squall Line, a Tropical Cyclone, and a Winter Storm. Monthly Weather Review, 141, 2390–2415, doi: 10.1175/MWR-D-12-00278.1, 2013.

Guo, F., Li, Y., Huang, Z., Wang, M., Zeng, F., Lian, C. and Mu, Y.:Numerical simulation of 23 June 2016 Yancheng City EF4 tornadic supercell and analysis of lightning activity. Science China Earth Sciences, 60, 2204-2213, doi: 10.1007/s11430-017-9109-8, 2017.

Hallett, J., and Mossop, S. C.: Production of secondary ice particles during the riming process. Nature, 249, 26–28, doi: doi: 10.1038/249026a0, 1974.

Heymsfield, A. and Willis, P.: Cloud conditions favoring secondary ice particle production in tropical maritime convection. J. Atmos. Sci., 71, 4500–4526, doi: 10.1175/JAS-D-14-0093.1, 2014.

Hong, S.-Y., Noh, Y., and Dudhia, J.: A New Vertical Diffusion Package with an Explicit Treatment of Entrainment Processes. Monthly Weather Review, 134, 2318–2341, doi: 10.1175/MWR3199.1, 2006.

James, R. L., Phillips, V. T. and Connolly, P. J.: Secondary ice production during the break-up of freezing water drops on impact with ice particles. Atmospheric Chemistry and Physics, 21, 18519-18530, doi: 10.5194/acp-21-18519-2021, 2021.

Jiménez, P. A., Dudhia, J., González-Rouco, J. F., Navarro, J., Montávez, J. P., and García-Bustamante, E.: A Revised Scheme for the WRF Surface Layer Formulation. Monthly Weather Review, 140, 898–918, doi: 10.1175/MWR-D-11-00056.1, 2012.

535   Jing, X., Yang, J., Li, T., Hu, J., He, C., Yin, Y., DeMott, P. J., Wang, Z., Jiang, H., Chen, K.: Pre-activation of ice nucleating particles in deposition nucleation mode: Evidence from measurement using a static vacuum water vapor diffusion chamber in Xinjiang, China. Geophysical Research Letters, 49, e2022GL099468, doi: 10.1029/2022GL099468, 2022.

Kain, J. S.: The Kain–Fritsch Convective Parameterization: An Update. Journal of Applied Meteorology, 43, 170–181, doi: 10.1175/1520-0450(2004)043<0170:TKCPAU>2.0.CO;2, 2004.

540   Khain, A., Pokrovsky, A., Pinsky, M., Seifert, A., and Phillips, V.: Simulation of Effects of Atmospheric Aerosols on Deep Turbulent Convective Clouds Using a Spectral Microphysics Mixed-Phase Cumulus Cloud Model. Part I: Model Description and Possible Applications. Journal of the Atmospheric Sciences, 61, 2963–2982, doi: 10.1175/JAS-3350.1, 2004.

King, W. D., and Fletcher, N. H.: Pressures and stresses in freezing water drops. Journal of Physics D: Applied Physics, 6, 2157–2173, doi: 10.1088/0022-3727/6/18/302, 1973.

545   Korolev, A., and Leisner, T.: Review of experimental studies of secondary ice production. Atmospheric Chemistry and Physics, 20, 11767–11797, doi: 10.5194/acp-20-11767-2020, 2020.

Latham, J., Blyth, A. M., Christian, H. J., Deierling, W., and Gadian, A. M.: Determination of precipitation rates and yields from lightning measurements. Journal of Hydrology, 288(1–2), 13–19, doi: 10.1016/j.jhydrol.2003.11.009, 2004.

Lauber, A., Kiselev, A., Pander, T., Handmann, P., and Leisner, T.: Secondary Ice Formation during Freezing of Levitated

550   Droplets. Journal of the Atmospheric Sciences, 75, 2815–2826, doi: 10.1175/JAS-D-18-0052.1, 2018

Li, J.; Dai, B.; Zhou, J.; Zhang, J.; Zhang, Q.; Yang, J.; Wang, Y.; Gu, J.; Hou, W.; Zou, B, and Li, J.: Preliminary Application of Long-Range Lightning Location Network with Equivalent Propagation Velocity in China. Remote Sens. 14, 560, doi: 10.3390/rs14030560, 2022.

Lyu, W., Zheng, D., Zhang, Y., Yao, W., Jiang, R., Yuan, S., Liu, D., Lyu, F., Zhu, B., Lu, G. and Zhang, Q.: A Review of

555   Atmospheric Electricity Research in China from 2019 to 2022. Advances in Atmospheric Sciences, 40, 1457-1484, doi: 10.1007/s00376-023-2280-x, 2023.

Mansell, E. R., MacGorman, D. R., Ziegler, C. L., and Straka, J. M., Charge structure and lightning sensitivity in a simulated multicell thunderstorm. Journal of Geophysical Research, 110, D12101, doi: 10.1029/2004JD005287, 2005.

Mansell, E. R.: On Sedimentation and Advection in Multimoment Bulk Microphysics. Journal of the Atmospheric Sciences,

560   67(9), 3084–3094, doi: 10.1175/2010JAS3341.1, 2010.

Michimoto, K.: A study of radar echoes and their relation to lightning discharge of thunderclouds in the Hokuriku district Part I: Observation and analysis of thunderclouds in summer and winter. Journal of the Meteorological Society of Japan. Ser. II, 69, 327-336, doi: 10.2151/jmsj1965.69.3_327, 1991.

Mlawer, E. J., Taubman, S. J., Brown, P. D., Iacono, M. J., and Clough, S. A.: Radiative transfer for inhomogeneous

565   atmospheres: RRTM, a validated correlated-k model for the longwave. Journal of Geophysical Research: Atmospheres, 102(D14), 16663–16682, doi: 10.1029/97JD00237, 1997.

Moore, C. B.: Rebound limits on charge separation by falling precipitation. Journal of Geophysical Research, 80, 2658–2662, doi: 10.1029/JC080i018p02658, 1975.

Phillips, V. T. J., Yano, Jun-Ichi, Khain, A.: Ice Multiplication by Breakup in Ice-Ice Collisions. Part I: Theoretical
570   Formulation. J. Atmos. Sci., doi: 10.1175/JAS-D-16-0224.1, 2017.

Phillips, V. T. J., Patade, S., Gutierrez, J., and Bansemer, A.: Secondary Ice Production by Fragmentation of Freezing Drops:
Formulation and Theory. J. Atmos. Sci., 75, 3031–3070, doi: 10.1175/JAS-D-17-0190.1, 2018.

Phillips, V. T., Formenton, M., Kanawade, V. P., Karlsson, L. R., Patade, S., Sun, J., Barthe, C., Pinty, J. P., Detwiler, A. G.,
Lyu, W. and Tessendorf, S. A.: Multiple environmental influences on the lightning of cold-based continental cumulonimbus
575   clouds. Part I: Description and validation of model. J. Atmos. Sci., 77, 3999-4024, doi: 10.1175/JAS-D-19-0200.1, 2020.

Phillips, V.T. and Patade, S.: Multiple Environmental Influences on the Lightning of Cold-Based Continental Convection. Part
II: Sensitivity Tests for Its Charge Structure and Land–Ocean Contrast. J. Atmos. Sci., 79, 263–300, dio: 10.1175/JAS-D-20-
0234.1, 2022.

Qie, X. S., and Zhang, Y. J.: A review of atmospheric electricity research in China from 2011 to 2018. Adv. Atmos. Sci., 36,
580   994−1014, doi: 10.1007/s00376-019-8195-x, 2019.

Qie, X. S., and Coauthors: A review of atmospheric electricity research in China. Adv. Atmos. Sci., 32, 169−191, doi:
10.1007/s00376-014-0003-z, 2015.

Saunders, C. P. R., and Peck, S. L.: Laboratory studies of the influence of the rime accretion rate on charge transfer during
crystal/graupel collisions. Journal of Geophysical Research: Atmospheres, 103, 13949–13956, doi: 10.1029/97JD02644, 1998.

585   Saunders, C. P. R., Peck, S. L., Aguirre Varela, G. G., Avila, E. E., and Castellano, N. E.: A laboratory study of the influence
of water vapour on the charge transfer process during collisions between ice crystals and graupel. Atmos. Res., 58, 187–203,
doi: 10.1016/S0169-8095(01)00090-4, 2001.

Shi, Z., Tan, Y. B., Tang, H. Q., Sun, J., Yang, Y., Peng, L., and Guo, X. F.: Aerosol effect on the land-ocean contrast in
thunderstorm electrification and lightning frequency. Atmospheric Research, 164–165, 131–141, doi:
590   10.1016/j.atmosres.2015.05.006., 2015.

Takahashi, T.: A numerical simulation of winter cumulus electrification. Part I: Shallow cloud. Journal of Atmospheric
Sciences, 40, pp.1257-1280, doi: 10.1175/1520-0469(1983)040<1257:ANSOWC>2.0.CO;2, 1983.

Takahashi, Nagao, Y., and Kushiyama, Y.: Possible High Ice Particle Production during Graupel–Graupel Collisions. J. Atmos.
Sci., 52(24), 4523–4527, doi: 10.1175/1520-0469(1995)052<4523:PHIPPD>2.0.CO;2, 1995.

595   Takahashi, T., Tajiri, T., and Sonoi, Y.: Charges on graupel and snow crystals and the electrical structure of winter
thunderstorms. J. Atmos. Sci., 56, 1561–1578, doi: 10.1175/1520-0469(1999)056<1561:COGASC>2.0.CO;2, 1999.

Takahashi, T. and Miyawaki, K.: Reexamination of riming electrification in a wind tunnel. J. Atmos. Sci., 59, 1018–1025, doi:
10.1175/1520-0469(2002)059<1018:ROREIA>2.0.CO;2, 2002.

Takahashi, T., Sugimoto, S., and Kawano, T.: Microphysical structure and lightning initiation in Hokuriku Winter Clouds.
600   XVI International Conference on Atmospheric Electricity, O-04-01, 17–22 June 2018, Nara city, Nara, Japan.

Takahashi, T., Sugimoto, S., Kawano, T., and Suzuki, K.: Microphysical structure and lightning initiation in Hokuriku winter
clouds. Journal of Geophysical Research: Atmospheres, 124, 13,156–13,181, doi: 10.1029/2018JD030227, 2019.

Tewari, M., Chen, F., Wang, W., Dudhia, J., LeMone, M. A., Mitchell, K., Ek, M., Gayno, G., Wegiel, J., and Cuenca, R. H: Implementation and verification of the unified NOAH land surface model in the WRF model, 20th Conference on Weather Analysis and Forecasting/16th Conference on Numerical Weather Prediction. American Meteorological Society: Seattle, WA, US, 11–15, 2004.

Wang, D., Zheng, D., Wu, T. and Takagi, N.: Winter positive cloud-to-ground lightning flashes observed by LMA in Japan. IEEJ Transactions on Electrical and Electronic Engineering, 16, 402-411, doi:10.1002/tee.23310, 2021

Xu, L. T., Zhang, Y. J., Wang, F., and Cao, X.: Simulation of inverted charge structure formation in convective regions of mesoscale convective system. J. Meteor. Soc. Japan, 97, 1119−1135, doi: 10.2151/jmsj.2019-062, 2019.

Yang, J., Wang, Z., Heymsfield, A., and Luo, T., Liquid-ice mass partition in tropical maritime convective clouds. J. Atmos. Sci., 73, 4959-4978, doi: 10.1175/JAS-D-15-0145.1, 2016.

Yang, J., Wang, Z., Heymsfield, A. J., DeMott, P. J., Twohy, C. H., Suski, K. J., and Toohey, D. W.: High Ice Concentration Observed in Tropical Maritime Stratiform Mixed-Phase Clouds with Top Temperatures Warmer than -8 °C. Atmos. Res., 233, 104719, doi: 10.1016/j.atmosres.2019.104719, 2020.

Yano, J.-I., and Phillips, V. T. J.: Ice–Ice Collisions: An Ice Multiplication Process in Atmospheric Clouds. Journal of the Atmospheric Sciences, 68, 322–333, doi: 10.1175/2010JAS3607.1, 2011.

Zhang, Y. J., and Coauthors: A review of advances in lightning observations during the past decade in Guangdong, China. J. Meteor. Res., 30, 800−819, doi: 10. 1007/s13351-016-6928-7, 2016.

Zheng, D., Wang, D., Zhang, Y., Wu, T., and Takagi, N.: Charge regions indicated by LMA lightning flashes in Hokuriku's winter thunderstorms. Journal of Geophysical Research: Atmospheres, 124, doi: 10.1029/2018JD030060, 2019.